ACS APPLIED MATERIALS & INTERFACES

www.acsami.org

Research Article

Controlled *p*-Type Doping of Pyrite FeS_2

Bryan Voigt, Lis Stolik Valor, William Moore, Jeff Jeremiason, James Kakalios, Eray S. Aydil,* and Chris Leighton*

Cite This: *ACS Appl. Mater. Interfaces* 2023, 15, 28258−28266

Read Online

ACCESS | Metrics & More | Article Recommendations | Supporting Information

ABSTRACT: Pyrite FeS_2 has extraordinary potential as a low-cost, nontoxic, sustainable photovoltaic but has underperformed dramatically in prior solar cells. The latter devices focus on heterojunction designs, which are now understood to suffer from problems associated with FeS_2 surfaces. Simpler homojunction cells thus become appealing but have not been fabricated due to the historical inability to understand and control doping in pyrite. While recent advances have put S-vacancy and Co-based *n*-doping of FeS_2 on a firm footing, unequivocal evidence for bulk *p*-doping remains elusive. Here, we demonstrate the first unambiguous and controlled *p*-type transport in FeS_2 single crystals doped with phosphorus (P) during chemical vapor transport growth. P doping is found to be possible up to at least ∼100 ppm, inducing ∼10^{18} holes/cm^3 at 300 K, while leaving the crystal structure and quality unchanged. As the P doping is increased in crystals natively *n*-doped with S vacancies, the majority carrier type inverts from *n* to *p* near ∼25 and ∼55 ppm P, as detected by Seebeck and Hall effects, respectively. Detailed temperature- and P-doping-dependent transport measurements establish that the P acceptor level is 175 ± 10 meV above the valence band maximum, explain details of the carrier inversion, elucidate the relative mobility of electrons and holes, reveal mid-gap defect levels, and unambiguously establish that the inversion to *p*-type occurs in the bulk and is not an artifact of hopping conduction. Such controlled bulk *p*-doping opens the door to pyrite *p*−*n* homojunctions, unveiling new opportunities for solar cells based on this extraordinary semiconductor.

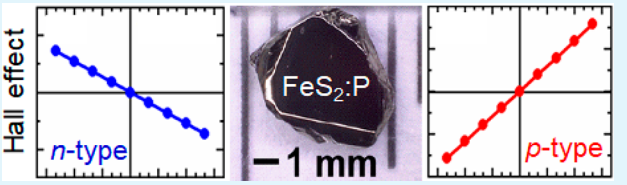

KEYWORDS: *pyrite, photovoltaics, semiconductors, p-type doping, homojunction solar cells*

INTRODUCTION

In many parts of the world, renewable electrical power from various sources is already cost-competitive with traditional fossil-fuel-based sources.[1] Notwithstanding the progress with curbing of CO_2 emissions that such renewable power sources enable, many energy sustainability challenges remain. Considering solar power, for example, over 90% of current solar cells utilize Si as a photovoltaic.[2−4] Si absorbs sunlight relatively poorly, however, necessitating thick absorbers in solar cells, and thus large quantities of Si, which typically require energy-intensive processing.[2−4] While alternative photovoltaic technologies based on *thin-film* absorbers such as CdTe, $Cu(In,Ga)Se_2$, and halide perovskites have progressed rapidly,[2−4] these raise clear concerns related to the cost (e.g., for In), elemental abundance (Cd, Te, In, Se), and/or toxicity (e.g., Cd, Pb) of their constituents. This situation has motivated much research on developing alternative low-cost, nontoxic, earth-abundant, thin-film absorbers, potentially better suited to TW-scale deployment.[2−5] Of the numerous candidates, pyrite-structure FeS_2 is uniquely attractive.[5] Pyrite has a 0.95 eV band gap, theoretical solar cell efficiency ∼30%, extreme visible light absorbance, high minority-carrier lifetime, etc.,[6] while being composed of exceptionally abundant, inexpensive, and nontoxic elements.[5] This rare combination renders pyrite very attractive for large-scale photovoltaics.

Despite this potential and more than 30 years of research, pyrite-based solar cells have disappointed.[6,7] A glaring, persistent problem with pyrite has been the inability to understand and control doping (e.g., refs 6 and 8−17), which precluded the simplest potential route to pyrite-based solar cells, namely *p*−*n* homojunctions. This situation forced researchers to turn to *heterojunction* solar cell designs (e.g., Schottky devices[6,7,18−20]), which have consistently underperformed, yielding power conversion efficiencies typically below ∼3%, primarily due to low open-circuit voltages (<0.3 V).[6,7,18−20] While the cause of these poor efficiencies has historically been debated,[6,7,18−20] several research groups recently arrived at essentially the same conclusion:[13,14,21−23] single-crystal pyrite has a nanoscopic (1−3 nm thick) *p*-type surface inversion layer,[13,14,21−23] which, in combination with the typically unintentionally doped *n*-type interior (due to S vacancies (V_S)[24]), creates an internal *p*−*n* junction.[13,14,21−23] This internal junction suffers from a high concentration of

Received: April 1, 2023
Accepted: May 19, 2023
Published: June 2, 2023

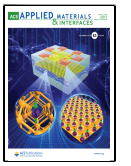

https://doi.org/10.1021/acsami.3c04662
ACS Appl. Mater. Interfaces 2023, 15, 28258−28266

mid-gap defects (again a consequence of poor understanding and control of doping and defects), which limits the open-circuit voltage and efficiency in devices such as FeS_2/metal Schottky solar cells.[13,23] *Homojunction* solar cells, which do not rely on pyrite surfaces or heterointerfaces, could circumvent these problems but require greatly improved understanding and control of doping, spanning both *n*- and *p*-type.

While historically challenging, doping of pyrite is gradually yielding to understanding. One example is the resolution of the so-called "doping puzzle" in FeS_2, which refers to the consensus that unintentionally doped thin films are typically *p*-type, whereas analogous single crystals are almost always *n*-type.[6−24] This was resolved only a few years ago via a large-scale study of the majority carrier type (from both Seebeck and Hall effects) in >100 pyrite crystals and films.[17] This study revealed that unintentionally doped pyrite is in fact nearly universally *n*-type,[17] regardless of the bulk or film nature, the *apparent* *p*-type behavior in low-mobility (<1 $cm^2\ V^{-1}\ s^{-1}$) films actually arising due to an artifact of hopping conduction.[11,17] In essence, as in a-Si:H, both the Seebeck and Hall effects can be artificially inverted in low-mobility samples;[11,17] pyrite thin films often exhibit low mobility due to uncontrolled heavy doping.[6−9,15,17] Some of the current authors went on to establish that V_S, long *suspected* to be important in pyrite,[6] are indeed the source of the unintentional *n*-doping.[24] Pyrite crystals grown by chemical vapor transport (CVT) in widely varied S vapor pressures exhibited unambiguous correlations with free electron density, resistivity, and mobility, realizing an approach to the insulator−metal transition (IMT) at high $[V_S]$.[24] This constitutes controlled V_S doping, at least in bulk crystals, additionally establishing that the native V_S donor level is deep, ∼225 meV below the conduction band minimum,[24] likely limiting the above-mentioned internal *p*−*n* junction.[13,23] Yet more recently, density functional theory studies suggested that the V_S-based defects inducing native *n*-doping are likely V_S *clusters* rather than isolated V_S.[25] In addition to V_S, Co is also known to *n*-dope pyrite, in this case via shallow donors.[23,26]

In sharp contrast to the above, well-understood and controlled *p*-doping of pyrite remains far from established. As already noted, the vast majority of prior thin-film claims of *p*-type pyrite have to be questioned due to likely contamination by low-mobility inversion of the Seebeck and/or Hall effects.[17] In bulk crystals, *p*-doping is also on shaky ground. As, Sb, and P have been *suggested* to be *p*-dopants,[6,27−34] but the evidence is limited, scattered, and frequently contradictory, with controlled *p*-doping not established. In naturally occurring pyrite crystals, findings are widely variable, and most observations indicate *n*-type behavior, although occasional *p*-type behavior is reported, often associated with As or P impurities.[27−31] In synthetic crystals, deliberate doping with P and As has been performed in attempts to *p*-dope pyrite, but with widely varying outcomes.[27,29,30,32−34] Both *n*- and *p*-type behaviors are reported, typically based on Hall or Seebeck effect data alone.[27,29,30,32−34] In cases where both are measured, the signs of the two effects often do not agree on *p*-type majority carriers.[32] Dopant concentrations are also often not quantified,[32,33] surface conduction is often not considered (meaning that any *p*-type behavior is difficult to associate with the pyrite bulk),[27−33] and the possibility of the typically low *p*-type mobilities[27−34] artificially inverting Hall and/or Seebeck effects[11,17] was not considered. There are thus many unresolved issues with *p*-type doping of pyrite. With this poor understanding and control of *p*-doping in pyrite FeS_2, the homojunction solar cells that could circumvent the now-established problems with heterojunctions have never been possible.

In light of the above, here we present a detailed study of phosphorus doping of pyrite FeS_2 single crystals, combining CVT growth, inductively coupled plasma mass spectrometry (ICPMS), powder X-ray diffraction (PXRD), high-resolution single-crystal X-ray diffraction (SCXRD), temperature-dependent (magneto)transport, and thermopower measurements. P was selected due to (i) the expectation that substitution of Group V P for Group VI S could lead to *p*-doping; (ii) the low toxicity of P relative to, e.g., As; (iii) the relatively similar ionic sizes of P and S; (iv) the known stability of pyrite-structure compounds such as CoSP,[35] where P substitutes S in pyrite CoS_2; and (v) the similar vapor pressure characteristics of P and S, which bodes well for P incorporation in CVT growth. P incorporation is indeed detected by ICPMS in CVT-grown FeS_2. As the P doping is increased in crystals natively *n*-doped with S vacancies, the majority carrier type is found to invert from *n* to *p* near 25 and 55 ppm of P, as detected by the Seebeck and Hall effects, respectively. P doping is then found possible up to at least ∼100 ppm, inducing $\sim 10^{18}$ holes/cm^3 at 300 K while leaving the crystal structure and quality unchanged. Detailed temperature- and P-doping-dependent transport measurements establish that the P acceptor level is 175 ± 10 meV above the valence band maximum, explain details of the carrier inversion, elucidate the relative mobility of electrons and holes, reveal mid-gap defect levels, and unambiguously establish that the inversion to *p*-type occurs in the *bulk* and cannot be an artifact of hopping. This provides unequivocal evidence for controlled *p*-type doping of FeS_2, opening the door to *p*−*n* homojunctions and unveiling new opportunities for solar cells based on this extraordinary semiconductor.

EXPERIMENTAL METHODS

CVT was used to grow the pyrite FeS_2 single crystals studied in this work. As alluded to above, we previously published extensive growth details and characterization of FeS_2 crystals with V_S doping controlled by the S:Fe loading in the CVT growth ampules,[23,24] forming the basis for the current study. The base growth employed 2.2 g of polycrystalline FeS_2 powder as a precursor (synthesized by sulfidation of 99.998% Fe (Alfa Aesar) with 99.9995% S (Alfa Aesar)), along with 100 mg of $FeBr_2$ (99.999%, Sigma-Aldrich) as a vapor transport agent.[23,24] No excess S was loaded, i.e., the S:Fe loading was close to 2.[23,24] Our prior work utilized X-ray diffraction, energy-dispersive X-ray and particle-induced X-ray emission spectroscopies, ICPMS, and time-of-flight secondary ion mass spectrometry, in conjunction with *T*-dependent transport to thoroughly characterize these crystals,[17,22−24,26] which have the largest electron mobilities reported for FeS_2.[26] Concentrations of Co (a known *n*-dopant[23,26]) are of order 1 ppm,[22−24,26] and V_S doping can be controlled down to electron densities (*n*) of 10^{15}−10^{16} cm^{-3} at 300 K, corresponding to donor concentrations of $\sim 10^{19}$ cm^{-3}.[22−24,26]

To intentionally P-dope such crystals, the base CVT process was adapted by spiking growth ampules with 1.5−113 mg of red P (99.999+%, Sigma-Aldrich).[33] The molar ratio of P to S loaded into the ampules (in at. %) is hereafter termed the "P loading". After evacuation (to $\sim 10^{-6}$ Torr) and flame sealing, the precursors (FeS_2, $FeBr_2$, and P) were shifted to one end of the ampules, which were placed in a multizone furnace. After a 3-day temperature inversion to clean the growth zone, CVT proceeded for 13 days, with hot and cold zones at 670 and 590 °C.[17,22−24,26] As noted above, P and S have similar vapor pressure characteristics, meaning that significant P

https://doi.org/10.1021/acsami.3c04662
ACS Appl. Mater. Interfaces 2023, 15, 28258−28266

incorporation is expected. At 630 °C, for example, P and S saturation vapor pressures are ∼6 and ∼9 atm, respectively.[36]

To assess impurity concentrations (including P) via ICPMS, CVT-grown crystals with mass >15 mg were first ground and digested overnight in 2.0 mL of ULTREX II nitric acid and 0.5 mL of ULTREX II hydrochloric acid. 0.5 mL aliquots of digestate were then diluted 20 times with Milli-Q deionized water (to decrease the acid content to ∼5 vol %) and analyzed in an Agilent 7700x ICPMS. PXRD data on ground crystals were acquired in a Rigaku MiniFlex 600 diffractometer equipped with a Cu X-ray source and graphite diffracted-beam monochromator to assess phase purity. The lattice parameter (a) was extracted by the method based on a linear fit of the extracted lattice parameter from each peak vs $\cos^2\theta/\sin\theta$.[37] For SCXRD, electronic transport, and thermopower measurements, large crystal facets were first visually identified and polished from both sides using progressive grinding to 1500-grit SiC sandpaper, followed by polishing with 3 and 1 μm diamond slurries. SCXRD data, including rocking curves, were then acquired with monochromated Cu $K\alpha_1$ radiation on a Panalytical X'Pert Pro diffractometer.

Soldered In contacts were used for four-terminal van der Pauw transport measurements[17,22−24,26] in a Quantum Design PPMS with a 9 T superconducting magnet. DC measurements employed a Keithley 2400 source-measure unit or a combination of a Keithley 220 current source with a Keithley 2002 voltmeter. AC measurements (at lower resistances) employed a Linear Research LR-700 AC resistance bridge. Thermopower (i.e., Seebeck effect) measurements were done in a home-built system at ∼30 mTorr and 330 K average temperature. Coplanar, 2-mm-gapped, 200-nm-thick Al electrodes were first evaporated onto thin (<200 μm thick) crystals, which were then placed across thermally isolated Cu blocks, also separated by 2 mm, such that the Al electrodes aligned with the Cu blocks. Each block has an embedded 50 W cartridge heater and anchored Pt thermometer, and the block temperatures were maintained to within ±50 mK of the set points using a Lake Shore 336 temperature controller. The average temperature ($T_{avg} = (T_1 + T_2)/2$) was maintained at 330 K while temperature gradients ($\Delta T = T_2 - T_1$) between ±8 and 0 K were sampled. Cu-wire probes made contact to the Al electrodes, and thermoelectric voltages were measured with a Keithley 617 electrometer.

RESULTS AND DISCUSSION

CVT growth of pyrite single crystals (see Figure 1d, left inset, for a photograph) was found possible at all P loadings attempted, up to 10 at. %. Again, this refers to the P/S loading in the growth ampules, not the actual P content incorporated into crystals. The actual P concentration from ICPMS is shown vs the growth ampule P loading in Figure 1a, where the ICPMS P detection limit of ∼5 ppm is shown as a horizontal dashed line. Between 0.1 and 1 at. %, the incorporated [P] from ICPMS scales as the P loading to the power 1.2 (this is a $\log_{10}$−$\log_{10}$ plot), the roughly linear relationship suggesting that P indeed incorporates from the vapor phase during CVT. The P concentration in these FeS_2 crystals can thus be controlled over a range of at least ∼7 ppm (essentially the detection limit) to ∼100−200 ppm, the sample-to-sample variations in Figure 1a being unsurprising at these concentration levels. Above 1 at. % P loading, the situation changes, with [P] essentially saturating at ∼100 ppm, the average [P] over all crystals between 1 and 10 at. % loading being 88 ppm. This indicates a doping limit at these growth conditions, although whether this is kinetic or thermodynamic is unclear. As detailed in the Supporting Information Section A (Table S1), ICPMS was also used to analyze 22 other impurities besides P. The ten most common were Ti, V, Cr, Mn, Co, Ni, Zn, Ge, Mo, and Sn, the typical concentrations of Co (a shallow donor in FeS_2[23,26]) being of order 1 ppm. Total metals-basis impurity concentrations exhibited inevitable

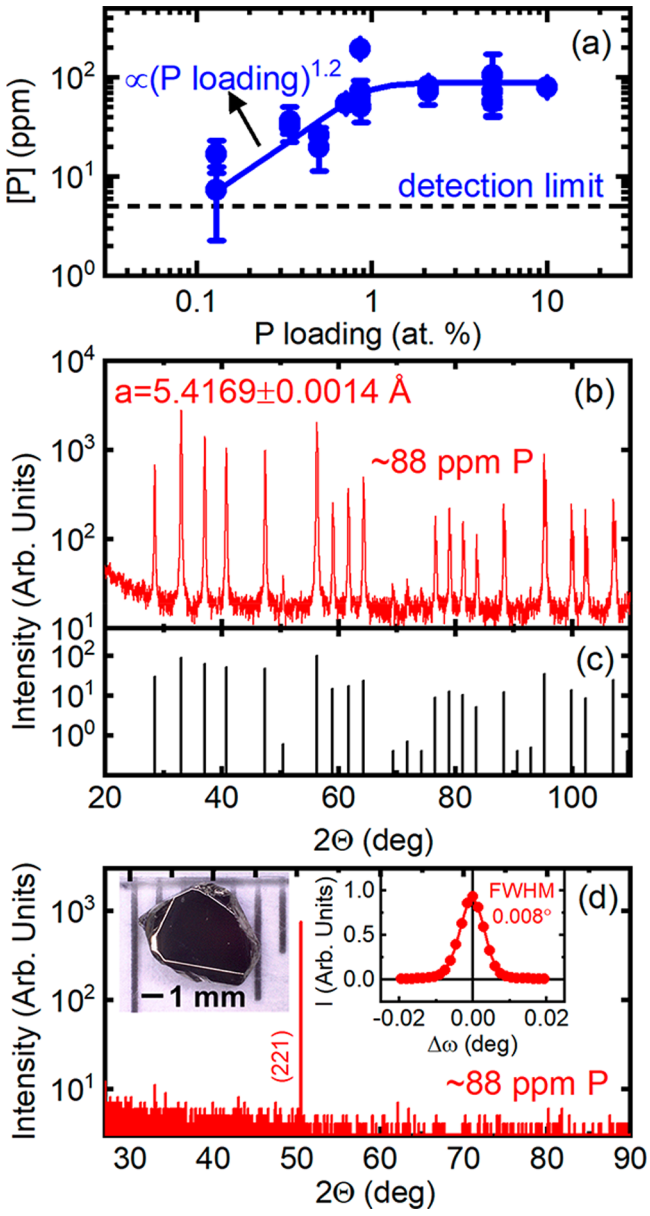

Figure 1. (a) Measured P concentration ([P], in (molar) parts per million, i.e., μmol/mol) in pyrite single crystals vs the P loading during chemical vapor transport growth. [P] is determined from inductively coupled plasma mass spectrometry (ICPMS), while the P loading is the molar ratio of P to S loaded into the growth ampules (in at. %). The solid blue line below 1 at. % is a power law fit to the data, smoothly joined to a saturated average [P] of 88 ppm above 1 at. %. The experimental ICPMS detection limit is marked as a horizontal dashed line. Multiple points at each P loading are different crystals, and the error bars correspond to the total uncertainty on each ICPMS measurement. (b) Wide-angle powder X-ray diffraction from a ground crystal (∼88 ppm P) with the extracted lattice parameter shown. (c) Reference pyrite X-ray diffraction pattern. (d) High-resolution wide-angle X-ray diffraction from a (221) facet of a single crystal. Right inset: rocking curve through the 221 peak, with a full width at half-maximum (FWHM) of 0.008°. Left inset: photograph of a polished, ∼88 ppm P crystal.

sample-to-sample variations but were mostly in the 20−100 ppm range. These findings are similar to prior reports of CVT growth of pyrite crystals from the highest purity precursors.[23,24,26] Importantly, neither the total impurity nor Co

https://doi.org/10.1021/acsami.3c04662
ACS Appl. Mater. Interfaces 2023, 15, 28258−28266

concentrations exhibited systematic variations with P doping (Table S1).

Extensive structural and chemical characterizations of crystals grown using our base CVT method (i.e., no P loading) have been published, establishing high-purity, high-quality, close-to-stoichiometric, phase-pure pyrite FeS_2 single crystals.[17,22−24,26] For comparison, Figures 1b−d provide PXRD and SCXRD data on crystals doped with ∼88 ppm of P, i.e., near our doping limit. The PXRD pattern in Figure 1b from a ground ∼88 ppm P-doped crystal very closely matches the pyrite FeS_2 reference pattern in Figure 1c, confirming phase purity. Moreover, the extracted cubic lattice parameter of a = 5.4169 ± 0.0014 Å is indistinguishable from non-P-doped crystals from our base CVT recipe (5.4165 ± 0.0014 Å[24]). Doping with ∼88 ppm P thus has a negligible impact on a, consistent with a recent report on the As-doping dependence of a in pyrite.[30] The single crystallinity of such P-doped samples is confirmed by the high-resolution SCXRD data in Figure 1d, which reveal only a sharp 221 reflection. This highlights an interesting difference between pure and P-doped crystals: the former typically present (111) and (100) facets,[17,22−24,26] whereas the latter often present higher-index facets such as the (221) apparent in Figure 1d and its left inset. This suggests that the P vapor pressure somehow changes the pyrite surface energetics and/or CVT growth kinetics. Interestingly, a change in the crystal habit of CVT-grown pyrite with P incorporation has been observed before.[33] As a final confirmation of structural quality, the right inset to Figure 1d presents an X-ray rocking curve through the 221 reflection, revealing a full width at half-maximum (FWHM) of only 0.008°. This very low mosaic spread is also indistinguishable from prior non-P-doped crystals from our base CVT method.[17,22−24,26]

With high-quality pyrite crystals with controlled P incorporation established, Figure 2 moves to the evolution of the majority carrier type with P doping. As alluded to in the Introduction, the Seebeck and Hall effects are the premier probes of majority carrier type in semiconductors and are most powerful when employed in tandem.[17] Figure 2 therefore shows the evolution of the near-room-temperature Seebeck (a−d) and Hall effects (e−h) with P doping. Figures 2e−h plot the transverse (Hall) resistance (R_{xy}) vs magnetic flux density (B), while Figures 2a−d plot the *negative* thermoelectric voltage ($-\Delta V$) vs temperature difference (ΔT). Plotting $-\Delta V$ enables direct comparison of the slope sign to the Hall effect; in this approach, n- and p-type crystals exhibit negative and positive slopes, respectively, in both Seebeck and Hall effects.

In crystals with no deliberate P doping (Figures 2a,e), for which ICPMS places an upper limit on [P] of ∼5 ppm, both the Seebeck (Figure 2a) and Hall (Figure 2e) slopes are clearly negative; i.e., the Seebeck coefficient (S) and Hall coefficient (R_H) are negative. This confirms electrons as majority carriers, i.e., n-type behavior, as expected due to native V_S doping.[23,24,26] As [P] is increased to ∼23 ppm (Figures 2b,f), however, R_H remains negative (Figure 2f) but S inverts to positive (Figure 2b), suggesting possible p-type behavior, even at this low P doping level. At ∼55 ppm P (Figures 2c,g), S then remains positive and increases in magnitude (Figure 2c), while R_H now also inverts to positive (Figure 2g), further evidencing an inversion to p-type behavior. At the highest [P] of ∼88 ppm (Figures 2d,h), positive S and R_H then persist, with S and R_H increasing and decreasing, respectively. This is exactly as expected for increased p-type doping; in the limit of

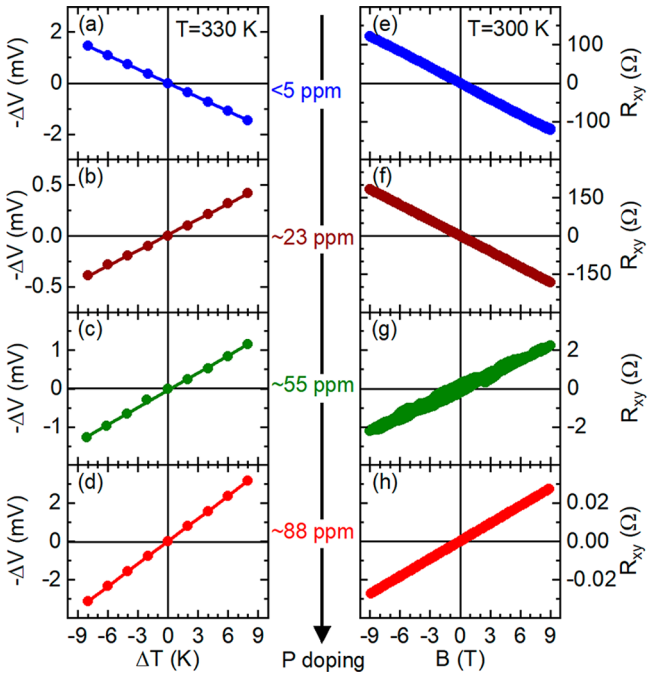

Figure 2. Evolution of the near-room-temperature Seebeck (left) and Hall (right) effects in representative pyrite single crystals with increasing P doping. [P] increases from <5 ppm (no intentional P doping, blue data, top) to ∼88 ppm (red data, bottom), with the [P] shown in each case. (a−d) 330 K temperature gradient (ΔT) dependence of the *negative* thermoelectric potential ($-\Delta V$). (e−h) 300 K magnetic flux density (B) dependence of the transverse (Hall) resistance (R_{xy}). Note that $-\Delta V$ is plotted in (a−d) to enable direct comparison of the slope sign to the Hall effect; in this approach, n- and p-type crystals exhibit negative and positive slopes, respectively, in both Seebeck and Hall effects. In all plots, the symbols are the experimental data, and the fitted straight lines provide the Seebeck and Hall coefficients.

dominant hole carriers, $R_H \rightarrow 1/(ep)$, where e is the electronic charge and p is the hole density, and so R_H decreases as p increases. Qualitatively, the *overall* behavior in Figure 2 is in fact as one would expect for true inversion of the majority carriers from electrons to holes, provided the electron mobility (μ_e) exceeds the hole mobility (μ_h). This situation would require higher P doping to invert the Hall effect (a transport probe) relative to the Seebeck effect (a thermodynamic probe), as the former would be skewed by $\mu_e > \mu_h$ while the latter would not, just as in Figure 2. Below, we directly confirm $\mu_e > \mu_h$, validating this picture. While all of the above points to true inversion of the majority carriers and P-induced p-type doping, based on the Introduction, it is essential to establish that this behavior is that of the pyrite *bulk* and that artifacts of hopping conduction can be ruled out. Temperature (T)-dependent measurements were thus performed.

Figure 3 shows the T dependence of the resistivity (ρ, Figures 3a,d,g,j), apparent electron or hole density ($1/|R_H|e$, Figures 3b,e,h,k), and Hall mobility (μ_H, Figures 3c,f,i,l) for four representative crystals with varied P doping. As for the remainder of this paper, electron carrier densities are shown as solid symbols and hole carrier densities as open symbols. Starting with no deliberate P doping (Figures 3a−c, "<5 ppm"), the behavior is n-type due to V_S doping, with $\rho(T)$, $n(T)$, and $\mu_H(T)$ in good accord with prior work.[17,22−24,26] $\rho(T)$ is insulating on cooling from 400 K, with a clear slope

https://doi.org/10.1021/acsami.3c04662
ACS Appl. Mater. Interfaces 2023, 15, 28258−28266

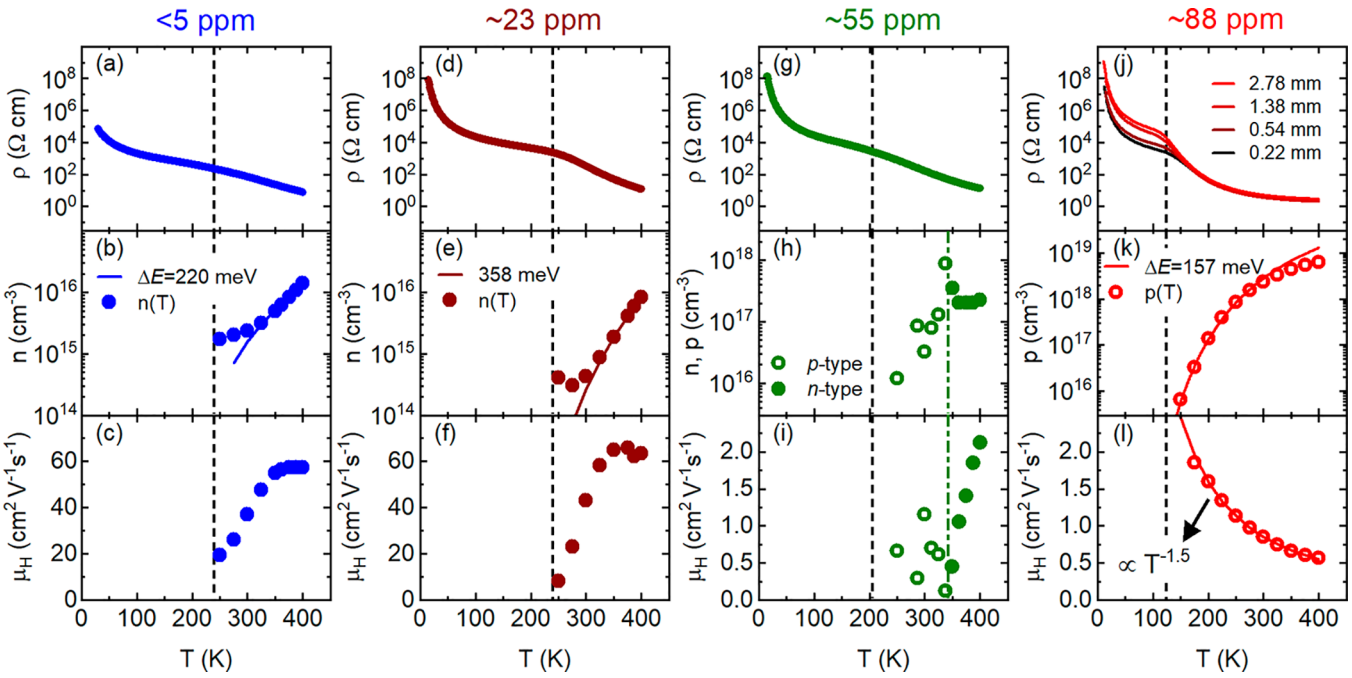

Figure 3. Temperature (T) dependence of the electronic transport properties of representative <5 ppm (a–c), ~23 ppm (d–f), ~55 ppm (g–i), and ~88 ppm (j–l) P-doped pyrite single crystals. Shown are the T dependence of the resistivity (ρ) (a, d, g, j), apparent Hall electron (n) and hole (p) densities (b, e, h, k), and Hall mobility (μ_H) (c, f, i, l). Filled and open symbols denote electron and hole majority carriers, respectively. The solid lines in (b, e, h, k) are Arrhenius fits described in the text. The solid line in (l) is a power law fit described in the text. In (j), the crystal thickness dependence is shown. In all cases, the crossover temperatures between bulk and surface transport are indicated with black vertical dashed lines. The T where bulk p–n inversion manifests in the Hall effect of the ~55 ppm P-doped crystal is shown with a green vertical dashed-dotted line in (i).

change reflecting the bulk-to-surface transport crossover.[14,17,22−24,26] Explicitly, the surface is more conductive than the bulk in single-crystal pyrite, meaning that when the bulk freezes out, the surface shunts current at sufficiently low T, inducing a crossover from bulk-dominated to surface-dominated transport.[14,17,22−24,26] The crossover occurs at ~240 K here (the vertical black dashed line), as can be precisely determined from Zabrodskii analysis (see Supporting Information Section B, Figure S1b, for examples).[38] Examining Figures 3a,d,g,j, the surface-to-bulk crossover is apparent at all P dopings. As expected, the crossover temperature varies (vertical black dashed lines), but crucially, in all cases it is safely below 300 K. This proves that the evolution in 300 K R_H with P doping in Figure 2 is truly reflective of a *bulk* inversion of the majority carrier type from n to p, i.e., true p-doping by P. This point is further emphasized in Figure 3j where $\rho(T)$ for a crystal with [P] ≈ 88 ppm is shown after polishing to four thicknesses between 2.78 and 0.22 mm. A clear thickness dependence evolves in the low-T regime but not at high-T, as expected for a surface-to-bulk crossover (the resistance is dependent on thickness for bulk transport but not surface transport).[14,17,22−24,26] Supporting Information Section B and Figure S1 provide additional details on the nature of the surface transport in heavily-P-doped crystals, from $\rho(T)$, $R_{xy}(B,T)$, and magnetoresistance; all findings are similar to prior work on crystals with no deliberate P doping,[17,22−24,26] indicating that the surface p-type layer arises in both cases. We note that the persistence of surface conduction into the regime where the interior is p-doped is not at all trivial. Rather, this indicates that the band bending generating p-type surface conduction in n-type crystals is maintained even in p-doped crystals, for reasons that are not entirely clear.

Moving to $n(T)$ and $p(T)$ (Figures 3b,e,h,k) and starting with no deliberate P doping (<5 ppm, Figure 3b), we find $n(300\ \mathrm{K}) = 2 \times 10^{15}$ cm^{-3}, i.e., light-to-moderate n-doping with V_S. Consistent with prior work,[17,22−24,26] $n(T)$ at high T is well described by simple activation, i.e., $n(T) = n_\infty \exp(-\Delta E/k_B T)$, where n_∞ is $n(T \to \infty)$, ΔE is a thermal activation energy, and k_B is Boltzmann's constant. The solid blue line in Figure 3b yields ΔE = 220 meV, very close to the 225 meV ionization energy previously deduced for V_S-related deep donors.[23,24,26] In the ~23-ppm-P-doped crystal (Figure 3e), $n(300\ \mathrm{K})$ decreases to 4×10^{14} cm^{-3}, implying that this level of P doping compensates some fraction of native V_S donors. $n(T)$ at high T is again activated, but with ΔE = 358 meV, i.e., increased activation energy compared to the nominally undoped case; this increase is meaningful and is discussed below. In the ~55 ppm P-doped crystal (Figure 3h), we now find a p-type Hall effect at 300 K (open symbols in Figure 3h), consistent with Figure 2g. The *apparent* hole density from $1/R_H e$ is ~10^{17} cm^{-3} but increases rapidly on warming, is notably noisy, then inverts to n-type above ~345 K (vertical green dashed-dotted line). This clearly indicates that this doping level lies very close to the compensation point marking the p–n crossover in the Hall effect. In the ~88 ppm P-doped crystal (Figure 3k), p-type behavior then becomes unambiguous in the Hall effect, $p(300\ \mathrm{K})$ reaching $\sim 2 \times 10^{18}$ cm^{-3}, i.e., quite heavy p-doping. From ~150 to ~300 K, $p(T)$ is also of activated form (solid red line), with ΔE = 157 meV, indicating that P is a moderately deep acceptor in pyrite. Above ~300 K, however, $p(T)$ begins to noticeably weaken relative to simple activation, likely indicating the onset of acceptor exhaustion. We note that the latter occurs at a p value approaching ~10^{19} cm^{-3}, roughly consistent with ~100 ppm P

https://doi.org/10.1021/acsami.3c04662
ACS Appl. Mater. Interfaces 2023, 15, 28258−28266

doping; lack of knowledge of the exact compensation level hinders further quantification.

Moving to $\mu_H(T)$ (Figures 3c,f,i,l), in the <5 and ~23 ppm P-doped crystals, which are *n*-type by Hall effect, $\mu_H(300\ K) \approx 40\ cm^2\ V^{-1}\ s^{-1}$, increasing with *T*. This is typical of lightly-V_S-doped pyrite crystals, which exhibit a maximum in $\mu_H(T)$ above 300 K due to competition between ionized impurity scattering and phonon scattering.[17,22−24,26] The mobility increases with *n*-doping in this regime (reaching as high as 2100 $cm^2\ V^{-1}\ s^{-1}$ below room temperature in prior work[26]), indicating that even these relatively high-purity crystals have significant disorder that is screened by increased electron density.[23,24,26] At ~55 ppm P doping (Figure 3i), around 300 K, the apparent hole mobility is low, no doubt responsible for the noisy $p(T)$ in Figure 3h. In the ~88 ppm P-doped crystal, however (Figure 3l), which exhibits a clear *p*-type Hall effect with well-behaved, activated $p(T)$, $\mu_H(T)$ systematically increases with decreasing *T* with a $T^{-1.5}$ dependence, reaching ~2 $cm^2\ V^{-1}\ s^{-1}$. This $\mu_H(T)$ unambiguously evidences phonon-limited *diffusive* hole transport, as does the simple activated $p(T)$ in Figure 3k and the >120 K form of $\rho(T)$ in Zabrodskii analysis (Figure S1b). The largest observed hole mobility of ~2 $cm^2\ V^{-1}\ s^{-1}$ is also 2 orders of magnitude larger than that at which a crossover to hopping conduction was previously observed in pyrite.[17] These ~88 ppm P-doped crystals thus exhibit clearly diffusive semiconductor transport, with no possibility of hopping conduction artificially inverting the sign of the Hall or Seebeck effects. The data of Figure 3 therefore confirm that the P-induced *p*-doping we observe is unequivocally associated with the pyrite bulk and not an artifact of hopping.

While large enough to confirm diffusive transport, the relatively low hole mobility of ~2 $cm^2\ V^{-1}\ s^{-1}$, which is reasonably consistent with prior reports,[27−34] is worthy of comment. This is, in fact, ~30 times smaller than the peak electron mobility in Figures 3c,f[17,22−24,26] and far smaller than the maximum electron mobility reported at any *T* in pyrite.[26] We note first that $\mu_e > \mu_h$ is not unexpected in pyrite FeS_2. First-principles electronic structure calculations indeed predict electron effective masses substantially lower than hole effective masses,[9,25,39] associated with a relatively narrow Fe 3*d* valence band, compared to a dispersive S 3*p* conduction band.[9,25,39] The extent of the difference in mobilities observed here, however (about a factor of 50 at 300 K), suggests that other factors are also at work, such as different electron−phonon scattering rates as well as the clear compensation we observe in *p*-doped samples due to V_S donors. Additional experimental and theoretical studies vs hole doping level would be worthwhile to explore these factors. Practically, however, we note that while $\mu_h \sim 1\ cm^2\ V^{-1}\ s^{-1}$ is low relative to μ_e in pyrite, this is nevertheless generally sufficient for the goal of *p*−*n* homojunction solar cells,[2−4,6] particularly with appropriate device design.

While Figures 1−3 already establish controlled *p*-doping of bulk pyrite to at least $p(300\ K) \sim 10^{18}\ cm^{-3}$, further insight can be obtained from deeper examination of the P doping dependence of transport, Hall, and Seebeck parameters. This is shown in Figure 4, where the 300 K apparent Hall carrier density ($1/|R_H|e$), 300 K μ_H, activation energy ΔE, and 330 K *S* are plotted vs [P] on a $\log_{10}$ scale. Multiple data points at single [P] values on these plots represent data from multiple crystals, providing a measure of sample-to-sample variations. Also, unintentionally P-doped crystals are plotted at 5 ppm

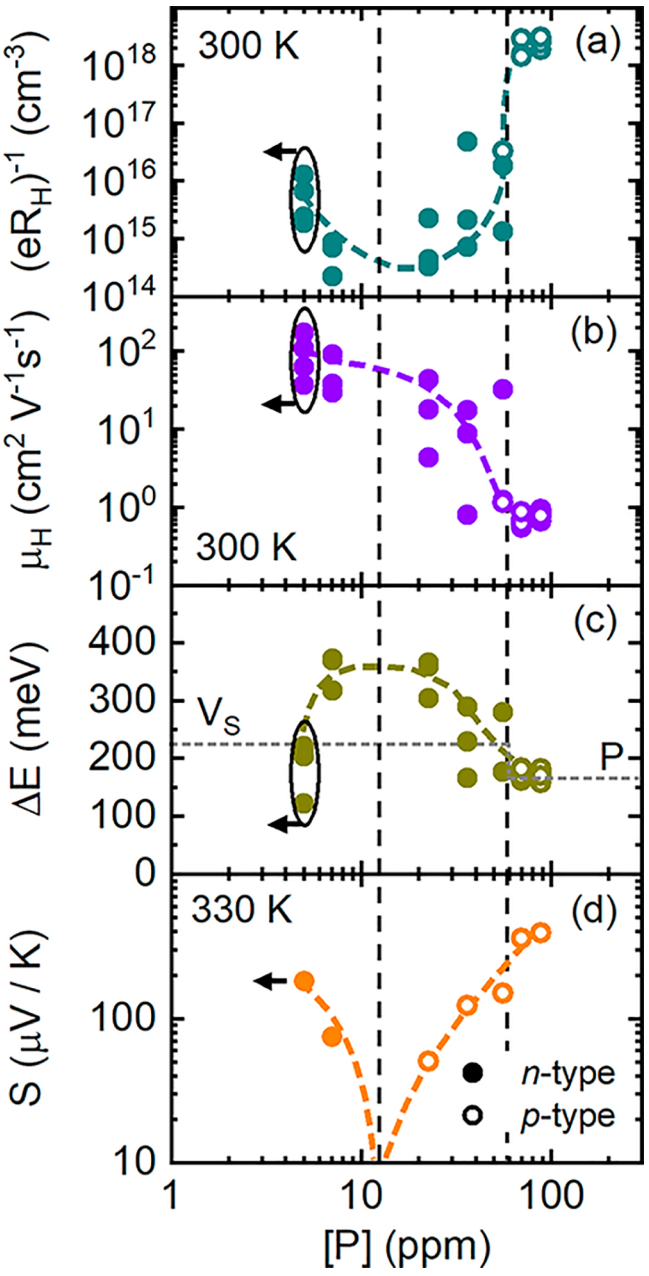

Figure 4. P concentration ([P]) dependence of (a) the 300 K apparent Hall carrier density (*n* or *p*), (b) the 300 K Hall mobility (μ_H), (c) the thermal activation energy (ΔE), and (d) the 330 K Seebeck coefficient (*S*). Filled and open symbols denote electron and hole majority carriers, respectively, determined via Hall (a−c) and Seebeck effects (d). Dashed lines are guides to the eye. Arrows attached to circled data indicate upper bounds on [P], i.e., points obtained from crystals beneath the ICPMS limit of detection for P. Multiple points at a single [P] are from multiple crystals. The vertical dashed lines mark the majority carrier type crossovers from the Seebeck (left) and Hall (right) effects.

(the ICPMS detection limit for P), with arrows pointing to lower P to indicate that these points represent upper bounds on [P].

Starting with the apparent 300 K carrier density (Figure 4a), all crystals with no intentional P doping are *n*-type, with *n*(300 K) in the 10^{15}−$10^{16}\ cm^{-3}$ range. As the P doping is increased, *n*(300 K) decreases to as low as $\sim 10^{14}\ cm^{-3}$ and stays low over quite a wide [P] range, reflecting clear compensation by P

https://doi.org/10.1021/acsami.3c04662
ACS Appl. Mater. Interfaces 2023, 15, 28258−28266

acceptors. At higher [P], the apparent n(300 K) then increases before inverting to p-type at ∼50 ppm P (the right vertical dashed line in Figure 4). Much like the T-driven situation in Figure 3h, the increase in apparent n(300 K) is expected, reflecting the fact that R_H goes through zero at the $n-p$ crossover, and we define the apparent carrier densities here as $1/|R_H|e$ for simplicity. Beyond the majority carrier type inversion point, all 12 of the ∼90 ppm P-doped crystals in Figure 4a exhibit p-type behavior with p(300 K) = (1−3) × 10^{18} cm^{-3}, demonstrating high reproducibility. Quantitatively, the fact that R_H inverts from n- to p-type at [P] as low as ∼50 ppm (∼4 × 10^{18} cm^{-3}) reveals an interesting detail. Specifically, this mid-10^{18} cm^{-3} acceptor concentration is quite low compared to the estimated V_S-related donor density in these crystals, which is in the 10^{19} cm^{-3} range.[23,24,26] This likely indicates that the background acceptor density in crystals natively n-doped by V_S is significant, consistent with the observation of μ_e increasing with n-doping in pyrite crystals due to screening of background charged defects (as discussed above in connection with Figures 3c,f).[23,24,26]

Moving to the 300 K μ_H (Figure 4b), the n-type crystals with no intentional P doping have μ_H of ∼30−200 cm^2 V^{-1} s^{-1}, consistent with Figures 3c,f and prior work.[17,22−24,26] μ_H is then relatively flat out to [P] ≈ 50 ppm, beyond which it collapses to ∼1 cm^2 V^{-1} s^{-1} in p-type crystals. As already noted, $\mu_e > \mu_h$ is expected in pyrite based on electronic structure arguments and explains the inversion of the sign of R_H at higher [P] (∼55 ppm) than the inversion of S (at ∼23 ppm) (see Figures 2 and 3b,e,h,k). Quantitatively, in the low-field limit of the two-carrier Hall effect, $R_H = \frac{1}{|e|}\frac{p\mu_h^2 - n\mu_e^2}{(p\mu_h + n\mu_e)^2}$, where μ_h and μ_e are the hole and electron Hall mobilities, respectively.[22,40] The mobility dependence in this expression renders R_H sensitive to the carriers with highest mobility (clearly electrons in pyrite), delaying the P-doping-induced inversion of R_H. In this sense the true inversion point, where $n = p = n_i$ (where n_i is the intrinsic carrier density), is better reflected in S than R_H, as reinforced below.[40]

Figure 4c shows the corresponding [P] dependence of the activation energy ΔE from $n(T)$ or $p(T)$ (see Figures 3b,e,h,k). Interestingly, the behaviors of ΔE in the heavily-n-doped and heavily-p-doped limits are relatively easily understood, while the intermediate behavior is more subtle. Specifically, crystals with no deliberate P doping have ΔE of ∼100−225 meV, reflecting the relatively deep V_S-related donor states,[23,24,26] while the average ΔE of the crystals with the highest [P] in Figure 4c is 175 ± 10 meV, revealing that P is a relatively deep acceptor in pyrite. These ΔE values in the n- and p-type cases are shown as the two horizontal gray dashed lines in Figure 4c. The intriguing finding is that at intermediate [P] ΔE clearly does not simply crossover from the n-type ΔE to the p-type ΔE. Instead, ΔE first increases significantly with increasing [P], reaching ∼370 meV, before dropping to the p-type ΔE near the Hall inversion point ([P] ≈ 55 ppm). Over a substantial [P] range, ΔE is thus pinned deep in the pyrite band gap, providing clear evidence of a widely distributed energy range of deep levels. Obvious origins of these levels include a distribution of deep donor states and a non-negligible concentration of background defects, both of which would be understandable in pyrite. The former has been predicted in the context of various possible V_S complexes,[25] while the latter would be again consistent with the observed increase in μ_e with n, implicating screening of a background of charged defects.[23,24,26]

Finally, Figure 4d shows the [P] dependence of the 330 K Seebeck coefficient, S. The n-type crystals with no deliberate P doping display relatively large, negative S values (solid points in Figure 4d indicate negative S, i.e., electrons as majority carriers) of around −180 μV K^{-1}, consistent with the >100 μV K^{-1} magnitudes reported at similar temperatures in several prior works (see ref 17 and references therein). S then remains negative until ∼10−20 ppm P (the left vertical dashed line in Figure 4), where it inverts before increasing to approximately +400 μV K^{-1} at the highest [P]. This provides a fuller view of the inversion of S discussed in connection with Figure 2, Figures 3b,e,h,k, and Figure 4a. As already noted, S inverts from n- to p-type before R_H due to the bias toward n-type carriers built into R_H because μ_e significantly exceeds μ_h; the inversion of S in Figure 4d therefore better reflects the true majority carrier type inversion from n to p with increasing P doping.[40] The rather large $S \approx 400$ μV K^{-1} deep in the p-doped region may then simply reflect the large effective mass and effective density of states in the valence band relative to the conduction band. As a final comment on these data, note that as in other semiconductors, pyrite should eventually exhibit a decrease in the magnitude of S at heavy n- and p-type doping due to the approach of the Fermi level to the conduction or valence band edge, respectively. This is likely not seen in Figure 4d due to the relatively deep nature of the donor and acceptor levels involved.

CONCLUSIONS

In summary, P doping of single crystals of pyrite FeS_2 has been achieved via chemical vapor transport growth. Inductively coupled plasma mass spectrometry, powder X-ray diffraction, single-crystal X-ray diffraction, temperature-dependent (magneto)transport measurements, and thermopower measurements were combined to generate a complete picture of the structural quality, purity, composition, and P-doping-dependent properties of such crystals. A clear evolution from native n-type doping due to S vacancies to p-type doping due to P substitution occurs as a function of P concentration. Both the Hall and Seebeck effects confirm that the majority carrier type inverts from electrons to holes, the full suite of measurements and analyses elucidating all aspects of this inversion. Vitally, the p-type behavior at higher P dopings was established to reflect the pyrite *bulk* (not the distinct surface layer) and is definitively associated with diffusive hole transport (not hopping). This unequivocally establishes P as a p-type dopant in pyrite FeS_2, enabling controlled p-doping. The P acceptor level was found to lie 175 ± 10 meV above the valence band maximum, and p-doping was demonstrated to 300 K hole densities up to ∼10^{18} cm^{-3}, at hole mobilities to ∼2 cm^2 V^{-1} s^{-1}.

The most important implications of these findings are clearly for pyrite photovoltaics. As described in the Introduction, the recent elucidation of the distinct electronic properties of pyrite's surface relative to its bulk[13,14,21−23] provides a coherent explanation for the poor performance of prior pyrite solar cells based on heterojunction designs.[6,7,18−20] Simpler homojunction solar cells now appear attractive but obviously require control of both n- and p-doping. This work establishes clear and controlled p-doping of pyrite for the first time, opening up the possibility of homojunction solar cells. Numerous fabrication approaches are possible, including P-vapor-based

https://doi.org/10.1021/acsami.3c04662
ACS Appl. Mater. Interfaces 2023, 15, 28258−28266

diffusion doping of *p*-type layers on *n*-type bulk crystals, "contact doping"[41,42] approaches to the same, or P ion implantation into crystals. Hybrid bulk crystal/thin-film designs are also possible, for example, depositing *n*-type films on *p*-type P-doped single crystals. Ultimately, the full potential of pyrite solar cells can only be realized in thin-film devices, meaning that an essential next step will be to control *p*-type doping in pyrite films also. For both thin films and crystals, it would additionally be desirable to understand any impacts of *p*-doping on the stability of pyrite.

Finally, we note that these findings are also relevant to pyrite *magnetism*, which is of growing interest.[39,43−45] While pure pyrite has $t_{2g}^6 e_g^0$, $S = 0$ electronic configuration and is thus diamagnetic, it has been known for some time that doping Co into pyrite in *n*-type $Fe_{1-x}Co_xS_2$ induces the onset of ferromagnetism at as little as $x \approx 0.01$,[43,45] eventually generating an itinerant ferromagnetic state at high x which is retained in CoS_2 (with Curie temperature near 120 K).[43−45] Remarkably, recent work demonstrated that a ferromagnetic state can be generated in pyrite not only by chemical doping with magnetic Co ions but also by electrostatic accumulation of a large surface density of electrons, *with no associated magnetic ions*, using electrolyte gating.[45] This was the first demonstration of voltage-induced ferromagnetism in a diamagnet.[45] Yet more recently, FeS_2 was predicted, based on first-principles calculations, to be a system in which *p*-doping from a diamagnetic state could induce ferromagnetism.[39] This is based on the narrow 3*d* valence band in FeS_2, enabling achievement of the Stoner criterion at relatively light *p*-doping, without magnetic dopants.[39] That work even predicted P as a potential dopant for this purpose.[39] The results presented here thus open up the exciting possibility of testing this prediction[39] through careful studies of the magnetic character of pyrite single crystals as a function of P doping.

■ ASSOCIATED CONTENT

Supporting Information

The Supporting Information is available free of charge at https://pubs.acs.org/doi/10.1021/acsami.3c04662.

Impurity analysis by ICPMS and additional electronic transport data (vs temperature and magnetic field) on P-doped FeS_2 single crystals (PDF)

■ AUTHOR INFORMATION

Corresponding Authors

Eray S. Aydil − *Department of Chemical and Biomolecular Engineering, New York University Tandon School of Engineering, Brooklyn, New York 11201, United States;* orcid.org/0000-0002-8377-9480; Email: aydil@nyu.edu

Chris Leighton − *Department of Chemical Engineering and Materials Science, University of Minnesota, Minneapolis, Minnesota 55455, United States;* orcid.org/0000-0003-2492-0816; Email: leighton@umn.edu

Authors

Bryan Voigt − *Department of Chemical Engineering and Materials Science, University of Minnesota, Minneapolis, Minnesota 55455, United States;* orcid.org/0000-0001-9308-7210

Lis Stolik Valor − *School of Physics and Astronomy, University of Minnesota, Minneapolis, Minnesota 55455, United States*

William Moore − *Department of Chemical Engineering and Materials Science, University of Minnesota, Minneapolis, Minnesota 55455, United States;* orcid.org/0000-0002-0407-5347

Jeff Jeremiason − *Department of Chemistry, Gustavus Adolphus College, Saint Peter, Minnesota 56082, United States;* orcid.org/0000-0003-3608-6793

James Kakalios − *School of Physics and Astronomy, University of Minnesota, Minneapolis, Minnesota 55455, United States*

Complete contact information is available at: https://pubs.acs.org/10.1021/acsami.3c04662

Author Contributions

C.L., E.S.A., and B.V. conceived the study; B.V. and W.M. synthesized and structurally characterized the FeS_2 single crystals under the supervision of C.L. and E.S.A.; B.V. and J.J. performed the ICPMS measurements and analysis; L.S.V. and J.K. performed the thermopower measurements; B.V. and W.M. performed the electronic transport measurements and analysis under the supervision of C.L. and E.S.A.; B.V., E.S.A., and C.L. wrote the paper, with input from all authors.

Notes

The authors declare no competing financial interest.

■ ACKNOWLEDGMENTS

This work was supported primarily by the Minnesota Environment and Natural Resources Trust Fund (ENRTF), as recommended by the Legislative-Citizen Commission on Minnesota Resources (LCCMR). Additional support was provided by the customers of Xcel Energy through a grant from the Renewables Development Fund. Thermopower measurements were supported by the National Science Foundation (NSF) through DMR-1608937. Parts of this work were performed in the Characterization Facility, University of Minnesota, which receives partial support from the NSF through the MRSEC (DMR-2011401) and NNCI (ECCS-2025124) programs. We thank D. Ray and L. Gagliardi for informative discussions and B. Das and M. Maiti for assistance.

■ REFERENCES

(1) International Energy Agency *Energy Technology Perspectives* 2023, IEA: Paris, https://www.iea.org/reports/energy-technology-perspectives-2023.

(2) Wolden, C. A.; Kurtin, J.; Baxter, J. B.; Repins, I.; Shaheen, S. E.; Torvik, J. T.; Rockett, A. A.; Fthenakis, V. M.; Aydil, E. S. Photovoltaic Manufacturing: Present Status, Future Prospects, and Research Needs. *J. Vac. Sci. Technol. A* **2011**, *29*, 030801.

(3) Haegel, N. M.; Atwater, H.; Barnes, T.; Breyer, C.; Burrell, A.; Chiang, Y.-M.; De Wolf, S.; Dimmler, B.; Feldman, D.; Glunz, S.; et al. Terawatt-scale Photovoltaics: Transform Global Energy. *Science* **2019**, *364*, 836.

(4) Nayak, P. K.; Mahesh, S.; Snaith, H. J.; Cahen, D. Photovoltaic Technologies: Analysing the State of the Art. *Nat. Rev. Mater.* **2019**, *4*, 269.

(5) Wadia, C.; Alivisatos, A. P.; Kammen, D. M. Materials Availability Expands the Opportunity for Large-scale Photovoltaics Deployment. *Environ. Sci. Technol.* **2009**, *43*, 2072.

(6) Ennaoui, A.; Fiechter, S.; Pettenkofer, C.; Alonso-Vante, N.; Büker, K.; Bronold, M.; Höpfner, C.; Tributsch, H. Iron Disulfide for Solar Energy Conversion. *Sol. Energy Mater. Sol. Cells* **1993**, *29*, 289.

(7) Steinhagen, C.; Harvey, T. B.; Stolle, C. J.; Harris, J.; Korgel, B. A. Pyrite Nanocrystal Solar Cells: Promising, or Fool's Gold? *J. Phys. Chem. Lett.* **2012**, *3*, 2352.

(8) Sun, R.; Chan, M. K. Y.; Kang, S. Y.; Ceder, G. Intrinsic Stoichiometry and Oxygen-induced p-type Conductivity of Pyrite FeS_2. *Phys. Rev. B* **2011**, *84*, 035212.
(9) Hu, J.; Zhang, Y.; Law, M.; Wu, R. First-principles Studies of the Electronic Properties of Native and Substitutional Anionic Defects in Bulk Iron Pyrite. *Phys. Rev. B* **2012**, *85*, 85203.
(10) Cabán-Acevedo, M.; Faber, M. S.; Tan, Y.; Hamers, R. J.; Jin, S. Synthesis and Properties of Semiconducting Iron Pyrite (FeS_2) nanowires. *Nano Lett.* **2012**, *12*, 1977.
(11) Zhang, X.; Manno, M.; Baruth, A.; Johnson, M.; Aydil, E. S.; Leighton, C. Crossover from Nanoscopic Intergranular Hopping to Conventional Charge Transport in Pyrite Thin Films. *ACS Nano* **2013**, *7*, 2781.
(12) Cabán-Acevedo, M.; Liang, D.; Chew, K. S.; DeGrave, J. P.; Kaiser, N. S.; Jin, S. Synthesis, Characterization, and Variable Range Hopping Transport of Pyrite (FeS_2) Nanorods, Nanobelts, and Nanoplates. *ACS Nano* **2013**, *7*, 1731−1739.
(13) Cabán-Acevedo, M.; Kaiser, N. S.; English, C. R.; Liang, D.; Thompson, B. J.; Chen, H.-E.; Czech, K. J.; Wright, J. C.; Hamers, R. J.; Jin, S. Ionization of High-density Deep Donor Defect States Explains the Low Photovoltage of Iron Pyrite Single Crystals. *J. Am. Chem. Soc.* **2014**, *136*, 17163.
(14) Limpinsel, M.; Farhi, N.; Berry, N.; Lindemuth, J.; Perkins, C. L.; Lin, Q.; Law, M. An Inversion Layer at the Surface of n-type Iron Pyrite. *Energy Environ. Sci.* **2014**, *7*, 1974.
(15) Zhang, X.; Scott, T.; Socha, T.; Nielsen, D.; Manno, M.; Johnson, M.; Yan, Y.; Losovyj, Y.; Dowben, P.; Aydil, E. S.; Leighton, C. Phase Stability and Stoichiometry in Thin Film Iron Pyrite: Impact on Electronic Transport Properties. *ACS Appl. Mater. Interfaces* **2015**, *7*, 14130.
(16) Shukla, S.; Xing, G.; Ge, H.; Prabhakar, R. R.; Mathew, S.; Su, Z.; Nalla, V.; Venkatesan, T.; Mathews, N.; Sritharan, T.; Sum, T. C.; Xiong, Q. Origin of Photocarrier Losses in Iron Pyrite (FeS_2) Nanocubes. *ACS Nano* **2016**, *10*, 4431.
(17) Zhang, X.; Li, M.; Walter, J.; O'Brien, L.; Manno, M. A.; Voigt, B.; Mork, F.; Baryshev, S. V.; Kakalios, J.; Aydil, E. S.; Leighton, C. Potential Resolution to the Doping Puzzle in Iron Pyrite: Carrier Type Determination by Hall Effect and Thermopower. *Phys. Rev. Mater.* **2017**, *1*, 015402.
(18) Büker, K.; Alonso-Vante, N.; Tributsch, H. Photovoltaic Output Limitation of n-FeS_2 (Pyrite) Schottky Barriers: A Temperature-dependent Characterization. *J. Appl. Phys.* **1992**, *72*, 5721.
(19) Ennaoui, A.; Fiechter, S.; Tributsch, H.; Giersig, M.; Vogel, R.; Weller, H. Photoelectrochemical Energy Conversion Obtained with Ultrathin Organo-metallic-chemical-vapor-deposition Layer of FeS_2 (Pyrite) on TiO_2. *J. Electrochem. Soc.* **1992**, *139*, 2514.
(20) Prabukanthan, P.; Thamaraiselvi, S.; Harichandran, G. Single Step Electrochemical Deposition of p-type Undoped and Co^{2+} Doped FeS_2 Thin Films and Performance in Heterojunction Solid Solar Cells. *J. Electrochem. Soc.* **2017**, *164*, D581.
(21) Liang, D.; Cabán-Acevedo, M.; Kaiser, N. S.; Jin, S. Gated Hall Effect of Nanoplate Devices Reveals Surface-state-induced Surface Inversion in Iron Pyrite Semiconductor. *Nano Lett.* **2014**, *14*, 6754.
(22) Walter, J.; Zhang, X.; Voigt, B.; Hool, R.; Manno, M.; Mork, F.; Aydil, E. S.; Leighton, C. Surface Conduction in *n*-type Pyrite FeS_2 Single Crystals. *Phys. Rev. Mater.* **2017**, *1*, 065403.
(23) Voigt, B.; Moore, W.; Maiti, M.; Walter, J.; Das, B.; Manno, M.; Leighton, C.; Aydil, E. S. Observation of an Internal p-n Junction in Pyrite FeS_2 Single Crystals: Potential Origin of the Low Open Circuit Voltage in FeS_2 Solar Cells. *ACS Materials Lett.* **2020**, *2*, 861.
(24) Voigt, B.; Moore, W.; Manno, M.; Walter, J.; Jeremiason, J. D.; Aydil, E. S.; Leighton, C. Transport Evidence for Sulfur Vacancies as the Origin of Unintentional n-type Doping in Pyrite FeS_2. *ACS Appl. Mater. Interfaces* **2019**, *11*, 15552.
(25) Ray, D.; Voigt, B.; Manno, M.; Leighton, C.; Aydil, E. S.; Gagliardi, L. Sulfur Vacancy Clustering and its Impact on Electronic Properties in Pyrite FeS_2. *Chem. Mater.* **2020**, *32*, 4820.
(26) Voigt, B.; Das, B.; Carr, D. M.; Ray, D.; Maiti, M.; Moore, W.; Manno, M.; Walter, J.; Aydil, E. S.; Leighton, C. Mitigation of the Internal p-n Junction in CoS_2-contacted FeS_2 Single Crystals: Accessing Bulk Semiconducting Transport. *Phys. Rev. Mater.* **2021**, *5*, 025405.
(27) Schieck, R.; Hartmann, A.; Fiechter, S.; Konenkamp, R.; Wetzel, H. Electrical Properties of Natural and Synthetic Pyrite (FeS_2) Crystals. *J. Mater. Res.* **1990**, *5*, 1567.
(28) Abraitis, P. K.; Pattrick, R. A. D.; Vaughan, D. J. Variations in the Compositional, Textural and Electrical Properties of Natural Pyrite: A Review. *Int. J. Miner. Process.* **2004**, *74*, 41.
(29) Lehner, S. W.; Savage, K. S.; Ayers, J. C. Vapor Growth and Characterization of Pyrite (FeS_2) Doped with Co, Ni, and As: Variations in Semiconducting Properties. *J. Cryst. Growth* **2006**, *286*, 306.
(30) Zuniga-Puelles, E.; Cardoso-Gil, R.; Bobnar, M.; Veremchuk, I.; Heide, G.; Gumeniuk, R. Electrical and Thermal Transport Properties of Natural and Synthetic $FeAs_xS_{2-x}$ ($x \leq 0.01$). *J. Phys. Chem. Sol.* **2021**, *150*, 109809.
(31) Wang, S.; Shen, J.; Du, B.; Xu, K.; Zhang, Z.; Liu, C. The Relationship Between Natural Pyrite and Impurity Element Semiconductor Properties: A Case Study of Vein Pyrite from the Zaozigou Gold Deposit in China. *Minerals* **2021**, *11*, 596.
(32) Willeke, G.; Blenk, O.; Kloc, Ch.; Bucher, E. Preparation and Electrical Transport Properties of Pyrite (FeS_2) Single Crystals. *J. Alloys Compd.* **1992**, *178*, 181.
(33) Blenk, O.; Bucher, E.; Willeke, G. P-type Conduction in Pyrite Single Crystals Prepared by Chemical Vapor Transport. *Appl. Phys. Lett.* **1993**, *62*, 2093.
(34) Lehner, S. W.; Newman, N.; van Schilfgaarde, M.; Bandyopadhyay, S.; Savage, K.; Buseck, P. R. Defect Levels and Electronic Behavior of Ni-, Co-, and As-doped Synthetic Pyrite (FeS_2). *J. Appl. Phys.* **2012**, *111*, 083717.
(35) Cabán-Acevedo, M.; Stone, M. L.; Schmidt, J. R.; Thomas, J. G.; Ding, Q.; Chang, H.-C.; Tsai, M.-L.; He, J.-H.; Jin, S. Efficient Hydrogen Evolution Catalysis Using Ternary Pyrite-type Cobalt Phosphosulphide. *Nat. Mater.* **2015**, *14*, 1245.
(36) *CRC Handbook of Chemistry and Physics*, 82nd ed.; Lide, D. R., Ed.; 2001; pp 6−69.
(37) Brandon, D.; Kaplan, W. D. *Microstructural Characterization of Materials*, 2nd ed.; Wiley: 2008; pp 85−90.
(38) Zabrodskii, A. G. The Coulomb Gap: The View of an Experimenter. *Philos. Mag. B* **2001**, *81*, 1131.
(39) Lei, B.-H.; Singh, D. J. Ferromagnetism in a Semiconductor with Mobile Carriers via Low-level Nonmagnetic Doping. *Phys. Rev. Appl.* **2021**, *15*, 044036.
(40) Ares, J.; Ferrer, I. J.; Sanchez, C. R. Majority Carriers in Pyrite Thin Films: An Analysis Based on Seebeck and Hall Coefficient Measurements. *Thin Solid Films* **2003**, *431*, 511.
(41) Ho, J. C.; Yerushalmi, R.; Jacobson, Z. A.; Fan, Z.; Alley, R. L.; Javey, A. Controlled Nanoscale Doping of Semiconductors via Molecular Monolayers. *Nat. Mater.* **2008**, *7*, 62.
(42) Hoarfrost, M. L.; Takei, K.; Ho, V.; Heitsch, A.; Trefonas, P.; Javey, A.; Segalman, R. A. Spin-on Organic Polymer Dopants for Silicon. *J. Phys. Chem. Lett.* **2013**, *4*, 3741.
(43) Guo, S.; Young, D. P.; Macaluso, R. T.; Browne, D. A.; Henderson, N. L.; Chan, J. Y.; Henry, L. L.; DiTusa, J. F. Discovery of the Griffiths Phase in the Itinerant Magnetic Semiconductor $Fe_{1-x}Co_xS_2$. *Phys. Rev. Lett.* **2008**, *100*, 017209.
(44) Wang, L.; Umemoto, K.; Wentzcovitch, R. M.; Chen, T. Y.; Chien, C. L.; Checkelsky, J. G.; Eckert, J. C.; Dahlberg, E. D.; Leighton, C. $Co_{1-x}Fe_xS_2$: A Tunable Source of Highly Spin-polarized Electrons. *Phys. Rev. Lett.* **2005**, *94*, 056602.
(45) Walter, J.; Voigt, B.; Day-Roberts, E.; Heltemes, K.; Fernandes, R. M.; Birol, T.; Leighton, C. Voltage-induced Ferromagnetism in a Diamagnet. *Sci. Adv.* **2020**, *6*, No. eabb7721.

https://doi.org/10.1021/acsami.3c04662
ACS Appl. Mater. Interfaces 2023, 15, 28258−28266